Citrate Assisted Synthesis of co-Doped ZnAl$_2$O$_4$ with La^{3+} and Pb^{2+} Ions and Applications; Adsorption–Photocatalysis

H. Filali[a,*], N. Boukheit[a], R. Bouhroum[b], W. Chekirou[a] and A. Karaali[a]

[a]*Laboratoire de Thermodynamique et Traitements de Surface des Matériaux,*
Université Frères Mentouri, Constantine 1, Route de Ain El-Bey, 25000, Constantine, Algeria
[b]*Laboratoire des Techniques Innovantes et Préservation de l'Environnement,*
Université Frères Mentouri Constantine 1, Route de Ain El-Bey, 25000, Constantine, Algeria

Samples of pure zinc aluminate (ZnAl$_2$O$_4$) and doped ZnAl$_2$O$_4$ with both lead (Pb^{2+}) at different ratios (0, 0.5, 1, 1.5, 2, 2.5 mol%) and a constant amount of lanthanum (La^{3+}: 1 mol%), were prepared by the citrate sol–gel technique, and then annealed at 900°C for 2 h. To study the structural, optical, and thermal properties, different characterization methods were used such as powder X-ray diffraction, scanning electron microscopy, energy-dispersive X-ray spectroscopy, differential scanning calorimetry, the Fourier transform infrared spectroscopy and the Raman spectroscopy. Analysis by X-ray diffraction revealed the presence, in all samples, of the cubic, single-phase ZnAl$_2$O$_4$ without any impurity phases, with a crystallite size between 19 and 25 nm. These results were confirmed using the Fourier transform infrared and the Raman spectroscopy. Also ultraviolet spectra indicated that the bandgap of the doped samples decreases and exhibits a redshift with increasing concentration of Pb^{2+} ion. In addition, the photocatalytic study for different samples of ZnAl$_2$O$_4$ showed that they could be used as photocatalysts and good adsorbents for the degradation of a hexamethyl crystallized violet dye in an aqueous solution.

topics: nanoparticles, sol–gel, photocatalysis, adsorption

1. Introduction

Zinc aluminate (ZnAl$_2$O$_4$) spinel has high thermal and chemical stabilities, high mechanical strength, low surface acidity [1, 2], and wide bandgap energy (3.8 eV) [3–6]. ZnAl$_2$O$_4$ powder with a large specific surface area and nanometric particle size make it the material of choice for a variety of applications, such as heterogeneous catalysis and adsorption of molecules [7, 8]. Also, zinc aluminate has been recently considered as a functional material in luminescent host applications [9]. Moreover, ZnAl$_2$O$_4$ has been widely used as a good phosphor host material as a result of uniform particle and narrow size distribution [10].

For effective doping, rare earth or lanthanides are amply used as activators in luminescent materials due to high emission properties [11, 12].

On the other hand, adsorption is a technique that fixes pollutants on the surface of an adsorbent without altering the pollutant. It is very often used as a refining treatment. Photocatalysis aims to eliminate organic micro pollution, but unlike adsorption, its ultimate goal is to degrade or even mineralize organic pollutants.

Moreover, zinc aluminate has been largely used as a photocatalyst for the degradation of organic pollutants in water such as dyes. Some studies involving the degradation of organic dyes using ZnAl$_2$O$_4$ as a photocatalyst are reported in the literature. Indeed, Foletto et al. [13] showed satisfactory photocatalytic activity of ZnAl$_2$O$_4$ particles for the degradation of a procion red dye in an aqueous solution. Also, ZnAl$_2$O$_4$ nanospheres synthesized by a wet solution chemical process showed good photocatalytic activity in the degradation of rhodamine B dye [14]. Under ultraviolet (UV) irradiation, a ZnO/ZnAl$_2$O$_4$ nanocomposite was evaluated for the photodegradation of a methyl orange dye [15], and ZnO/ZnAl$_2$O$_4$ microspheres exhibit great photodegradation performance for methylene blue compared to ZnO [16]. In our work, it was also tested as an adsorbent to remove the hexamethyl crystallized violet (HCV) dye. The crystal violet dye was considered as a low biodegradable and very persistent organic pollutant. Its presence in aquatic environments can be detrimental to animal and plant species, as well as to the various microorganisms living in these waters. Therefore, to evaluate the effectiveness of the synthesized ZnAl$_2$O$_4$ powder and

even in which area it can be used, the application in the field of water treatment was explored in terms of the suitability of the synthesized powders as photocatalysts to purify water from organic pollutants.

Many synthesis methods for the preparation of $ZnAl_2O_4$ have been reported, such as hydrothermal [17, 18], citrate [19–21], sol–gel [22–25], combustion [26–29], co-precipitation [30–32] and solvothermal [33, 34]. Doping with $ZnAl_2O_4$ was carried out with transition metals or rare-earth to obtain usable products with attractive properties depending on the intended application [35–38].

In the present study, we have used the citrate sol–gel method for preparing samples of pure $ZnAl_2O_4$ and dual doped $ZnAl_2O_4$, formed by a constant concentration of La^{3+} (1 mol%) and different contents $x\%$ of Pb^{2+} (0, 0.5, 1, 1.5, 2, 2.5 mol%). The materials were annealed at 900°C for 2 h and have been characterized for their structural and optical properties. In addition, we have prepared a sample $ZnAl_2O_4$ containing ZnO (50% by weight) to better characterize the effectiveness of the two purification methods, namely photocatalysis and adsorption.

2. Methods and materials

2.1. Synthesis of $ZnAl_2O_4$

To prepare the $ZnAl_2O_4$ powder, 2.19 g of $C_4H_6O_4Zn \cdot 2H_2O$ were mixed with 20 ml of distilled water and stirred magnetically for 30 min. On the other hand, another solution containing 7.5 g of $Al(NO_3) \cdot 9H_2O)$ and 20 ml of distilled water was prepared with the same preceding method. The two solutions were mixed thoroughly using $C_6H_8O_7$ as a chelating agent. The resulted mixture was dried on a hot plate at 80°C for 90 min. The doped $ZnAl_2O_4$ solutions were prepared exactly like pure. A constant amount of $(La(CH_3CO_2)_3 \cdot H_2O)$ (1 mol%) was added in the first solution of zinc. Different amounts of $C_4H_6O_4Pb \cdot 3H_2O$ were added to the second solution (0, 0.5,1, 1.5, 2 and 2.5 mol%). After drying the obtained mixture is subjected to a heat treatment at 900°C for 2 h in an oven. Finally, we have seven samples called pure $ZnAl_2O_4$, S0, S1, S2, S3, S4, and S5, respectively.

2.2. Photocatalysis and adsorption

To test the reactivity of the two methods on HCV molecules, several solutions each one containing 60 ml of HCV with a concentration equal to 5 mg/l g and 0.1 g from one sample of $ZnAl_2O_4$ powder were prepared. The readability of HCV was followed as a function of contact time by measuring the absorption at the maximum absorption length of HCV of 590 nm. To analyze photocatalytic activity, a cylindrical Pyrex photoreactor initiated by a UV mercury lamp (350 W) was placed in the center of a closed enclosure. The distance between the surface of the suspension and the light source was ≈ 20 cm. To establish the adsorption-desorption

equilibrium, the HCV solution and catalyst were stirred in the dark for 30 min at 500 rpm. During irradiation, samples were taken after each appropriate time interval. Next, 5 ml aliquots were taken and filtered using 0.22 μm membrane filters (S-PAK) to remove solid phases thus allowing analysis in the spectrophotometer (SHIMADZU, UV-1800).

2.3. Characterization

The obtained powder was characterized by X-ray diffraction (XRD) using a Cu K_α radiation Bruker (D8 Advance) X-ray diffractometer. The structural composition of powders was analyzed by an m-Raman spectrometer (Jobin-Yvon). Optical properties were carried out using a ultraviolet–visible (UV–Vis) spectrophotometer (Shimadzu, UV-1800). Morphological studies of the powders were carried out in a scanning electron microscope (Philips XL30 S-FEG). The Fourier transform infrared (FTIR) analysis was performed using a KBr disc technique on an FTIR spectrometer (Bruker IFS66v). Energy-dispersive X-ray spectroscopy (EDX) measurements have been performed with a Hitachi S-3000N scanning electron microscope and the thermal analysis of the dried gel was done in a TG/DS calorimeter (STA 449 F3 Jupiter®).

3. Results and discussions

3.1. Powder X-ray diffraction

Figure 1a shows XRD diffractograms of pure $ZnAl_2O_4$ and the S0, S1, S2, S3, S4, and S5 samples. All patterns show the characteristic diffraction peaks corresponding to the (111), (220), (311), (400), (331), (422), (511), (440), (620), (533), (642), (731) reflections of the cubic $ZnAl_2O_4$ spinel structure [39–41], and are consistent with the standard spectrum on JCPDS Card No. 05-0669. In addition, no diffraction peaks related to secondary phases or impurities were detected.
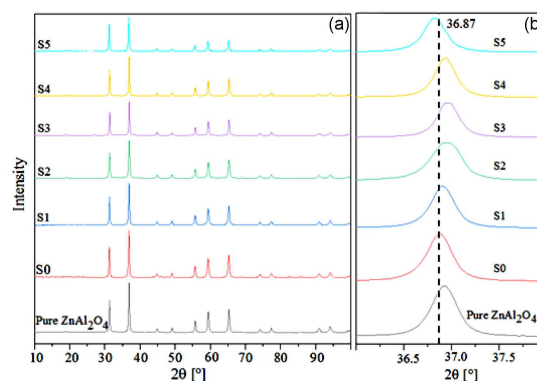

Fig. 1. (a) XRD diffractograms of all samples. (b) Shift of the most intense diffraction peak (311) of all samples.

TABLE I

Crystallinity, crystallite size, lattice parameter a, and lattice spacing d of all samples.

Samples	Crystallinity [%]	Crystallite size [nm]	a [Å]	d [Å]
pure $ZnAl_2O_4$	96	22	8.067	2.432
S0	94.5	23	8.080	2.436
S1	94	22	8.071	2.433
S2	94	19	8.063	2.431
S3	93	24	8.060	2.430
S4	94	25	8.065	2.432
S5	93	25	8.083	2.437

$ZnAl_2O_4$ is the only phase detected for all the samples. Therefore, these results indicate that all La^{3+} and Pb^{2+} ions successfully occupied the lattice sites in the $ZnAl_2O_4$ matrix. Furthermore, the sharp diffraction peaks show that the samples as prepared possess good crystallinity. The degree of crystallinity C [%] is calculated from the XRD spectra of the samples using

$$C = \frac{\text{area of crystalline peaks}}{\text{area of all peaks}} \times 100\% \qquad (1)$$

and the results are presented in Table I. The average crystallite size (D) was calculated from the five most intense X-ray diffraction peaks, using Scherrer's formula

$$D = \frac{0.9\lambda}{\beta \cos(\theta)}, \qquad (2)$$

where λ is the wavelength of Cu K_α (0.15406 nm), β is the full width at half maximum (FWHM) of the peak, and θ is the Bragg angle. We found an average crystallite size between 19 and 25 nm for S2 and S5, respectively (Table I). In addition, we noticed a slight shift of the most intense (311) diffraction peak of the S0 sample towards lower angles compared to pure $ZnAl_2O_4$. This suggests that the increase in the lattice parameter is most likely due to the presence of La^{3+} in the $ZnAl_2O_4$ matrix because the ionic radius of La^{3+} (1.04 Å) [42] is greater than those of the tetrahedral (Zn^{2+} (0.60 Å), Al^{3+} (0.39 Å)) and octahedral (Zn^{2+} (0.74 Å), Al^{3+} (0.54 Å)) sites of the $ZnAl_2O_4$ system [43].

The most intense diffraction peaks (311) for all samples are shown in Fig. 1b. We observe that the mechanism of the solid solution of $ZnAl_2O_4$ doped with Pb^{2+} must be different. This could include the formation of anion vacancies and the short-distance order phenomenon. Indeed, when Pb^{2+} (1.23 Å) [44], is added up to 1.5 mol% to the S0 sample, the most intense peak (311) moves towards larger angles, thus giving a contraction of the interplanar d-spacing. Similar results deviating from Vegard's law have been observed in metal alloys such as Ni–Cu, Au–Ag, Pd–Ag, Pt–Ag, and Ni–Co [45]. For example, Lubarda [46] observed similar results deviating from Vegard's law when replacing Au atoms (1.5939 Å) with Ag atoms (1.5969 Å), in an Au–Ag alloy.
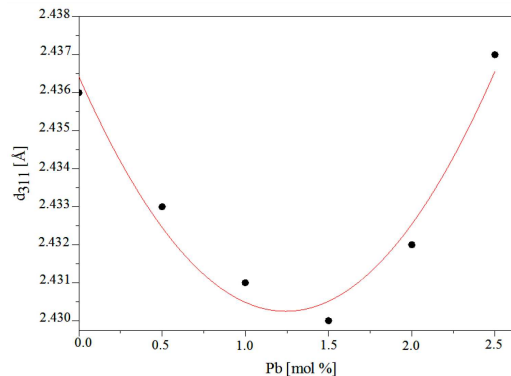

Fig. 2. The lattice spacing (d_{311}) versus the Pb percentage [%].

The lattice parameters (a) and lattice spacing (d) of the (311) diffraction peak for all samples are presented in Table I.

The variation of the lattice spacing of the (311) diffraction peak of the samples versus the Pb^{2+} % is represented in Fig. 2 and shows well the parabolic relationship. This result can be explained by the shrinkage of the Pb^{2+} outer electron shell due to its electronic interactions with the more numerous neighboring Zn^{2+} ions, which makes it smaller than the Zn^{2+} ion [47]. As the percentage of Pb^{2+} is increased further, the shrinkage is expected to be less pronounced (due to the additional Pb^{2+} ions), as a result, the lattice spacing is expected to recover or increase, which explains the increase in lattice spacing (d_{311}) at 2.5 mol% Pb^{2+}. Also, a similar phenomenon was observed by Motlung et al. [47], in $ZnAl_2O_4$ doped by Pb^{2+} ion. They found that the addition of 3.4% Pb^{2+} is an optimum for the compound to behave as expected by Vegard's law. On the other hand, in our study, 2.5 mol% (1% La^{3+} and 1.5% Pb^{2+}) are sufficient for Vegard's law to be verified. It is concluded that double doping could decrease the optimal value for which Vegard's law is satisfied.

3.2. FTIR spectroscopy

Figure 3 represents the FTIR spectra of pure $ZnAl_2O_4$ and the S0, S1, S2, S3, S4, and S5 samples recorded in the range 400–4000 cm^{-1}. We observe the same absorption bands in all spectra such as the broadband centered at 3400 cm^{-1} and the band at 1615 cm^{-1}. These are related to the O–H stretching vibration and H–O–H deformation vibration, respectively. Both of these can be assigned to water molecules on the surface of the samples [48].

The spinel-type structure can be confirmed by the bands at low energy (below 1000 cm^{-1}), which are related to the stretching and bending modes of the Al–O bonds. If Al^{3+} ions are in the octahedral sites of the six-coordinated AlO_6 group, the structure subsequently is normal spinel and
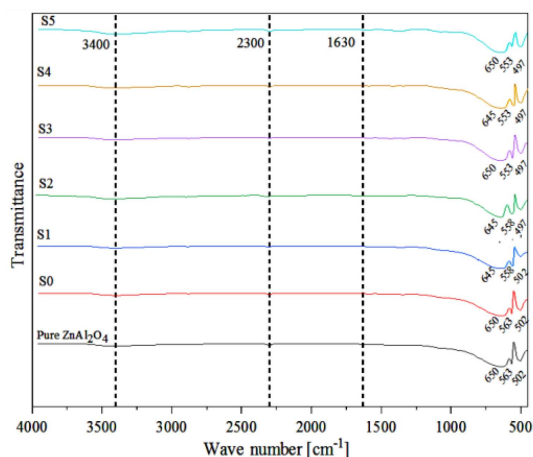
Fig. 3. FTIR spectra of all samples.

Fig. 4. TG, DSC, and DTG of pure $ZnAl_2O_4$.

the stretching and bending vibrations are expected at 500–700 cm^{-1} [49, 50]. It can be observed that the three absorption bands located at 501, (550–565), and 643 cm^{-1} come from the stretching and bending vibration modes of octahedral and tetrahedral bonds [51–53], which belong to the characteristic peaks of the spinel structure $ZnAl_2O_4$. Among them, the peak at 543 cm^{-1} corresponds to the symmetric bending vibration mode of the Zn–O bond in the A position of the tetrahedron, the peak at 643 cm^{-1} is attributed to the symmetric stretching vibration mode of the Al–O bond in the B position of the octahedron, while the weak band at 501 cm^{-1} is due to the asymmetric stretching mode of octahedral AlO_6 [54, 55]. The sharp absorption band at 2300 cm^{-1} is due to the stretching vibration mode of CO_2. The adsorption of water and carbon dioxide from the atmosphere may be due to the very high specific surface area of these materials [56]. No other impurity phase is detected by FTIR spectra and is in good agreement with the results obtained through XRD analysis.

3.3. TG and DSC

The behavior of the gel as a function of temperature was studied by continuous heating using simultaneously thermogravimetric analysis (TG) and differential scanning calorimetry (DSC). The thermal cycle applied under an atmosphere of neutral nitrogen consists of heating from ambient temperature to 1000°C at a speed of 10°C/min, followed by holding at this temperature for 10 min, and cooling to ambient temperature. The TG, DTG, and DSC patterns of pure $ZnAl_2O_4$ are recorded and depicted in Fig. 4. TG and DSC curves of all samples are almost similar. Thermogravimetric analysis reveals that the thermal decomposition of precursors takes place in four stages: The first loss of mass (4%) is observed between room temperature and 178°C. It probably corresponds to the dehydration of the gel (adsorbed water), evaporation of structural water, and decomposition of citric acid. The second
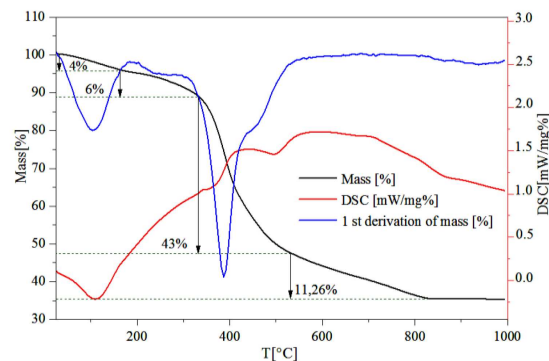
mass loss (6%), starts at 178°C and ends at 317°C. It can only be attributed to the decomposition of nitrates [56]. The third stage (317–548°C) reveals a significant mass loss ($\approx 43\%$) which is mainly due to the combustion of acetates and the removal of residual organic fragments formed during the heating. Finally, the last mass loss ($\approx 11\%$), begins at 548°C and ends at 826°C, corresponding to the removal of the hydroxyl groups. From 826°C, no loss of mass is observed, which shows that the crystallization of $ZnAl_2O_4$ is indeed complete. This approves our choice of 900°C as to the calcination temperature. The total weight loss is approximately 65% of the initial mass at 1000°C. Moreover, according to what is reported in the literature, the crystallization temperature of $ZnAl_2O_4$ strongly depends on the nature of the precursors and products used for the synthesis. For example, Ercan et al. [57] have shown that Ni-doped $ZnAl_2O_4$ nanopowders synthesized by using wet chemical method crystallize at 840°C. On DSC curves during heating, phase changes cause absorption or release of heat, which manifests as an endothermic (exothermic) peak during the reaction.

The DSC analysis curve shows the existence of several peaks:

- A large endothermic peak at 110°C corresponds to the evaporation of water.
- Two exothermic peaks; the first at 430°C can be attributed to the formation of aluminum and zinc oxide phases, and the second broad peak (548–826°C) is due to the formation of spinel $ZnAl_2O_4$.

We have also noticed that the increase in the quantities of Pb^{2+} leads to a small displacement of the peaks towards lower temperatures.

3.4. Raman analysis

The Raman spectroscopy is a characterization method to measure the frequencies of the long-wavelength lattice vibrations (phonons). The Raman spectroscopy provides a fast and convenient method for detecting small structural changes in materials. According to group theory,
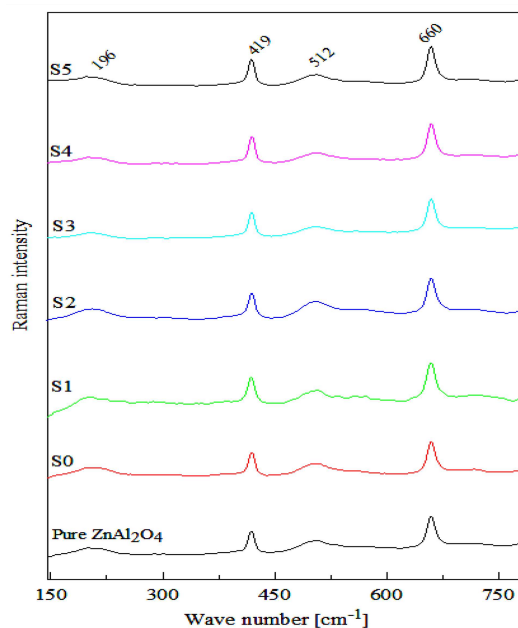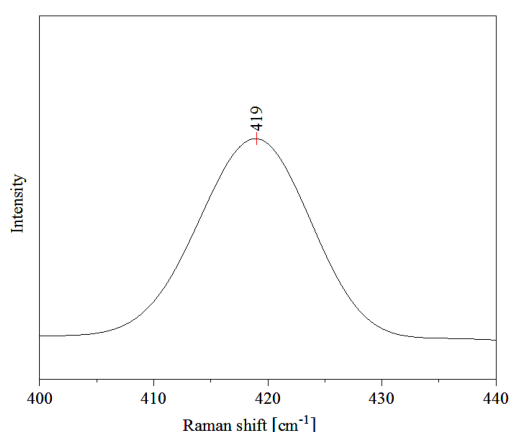
Fig. 5. Raman spectra of all samples.

Fig. 6. Symmetric Gaussian curve of the peak (419 cm^{-1}).

$ZnAl_2O_4$ should exhibit five Raman active modes: $A_{1g} + E_g + 3T_{2g}$ [58]. Figure 5 displays the Raman spectra of all the samples treated at 900°C for 2 h. These spectra are similar and reveal the presence of four peaks located at 196, 419, 512, and 660 cm^{-1} corresponding to T_{2g}, E_g, T_{2g}, and T_{2g} phonon frequencies of the $ZnAl_2O_4$ spinel structure, respectively [59–61]. In addition, peak T_{2g} (3) at 660 cm^{-1} is the most intense and represents the fingerprint of $ZnAl_2O_4$ spinel [62]. The peak located at 727 cm^{-1} corresponding to the active mode A_{1g} is not observed in our spectra. This peak is attributed to the symmetrical stretching vibration Al–O of the AlO_4 groups created by the redistribution of certain aluminum ions from the octahedral sites to the tetrahedral sites [63]. Also, Wang et al. [64] have shown a lower frequency Raman shift located in the 395–410 cm^{-1} and 630–650 cm^{-1} range which
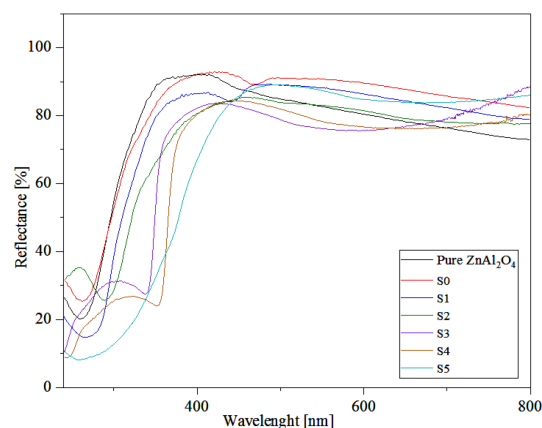

Fig. 7. The reflectance of all samples.

was attributed to the appearance of a minor inverse spinel structure. Furthermore, an inversion in the zinc aluminates could be indicated via an additional shoulder on the Raman E_g mode (420 cm^{-1}) [65]. However, in our Raman spectra, no other band is observed in the vicinity of this peak (see Fig. 6), indicating the absence of appreciable inversion in the spinel. Therefore, the $ZnAl_2O_4$ spinel formed in our samples has crystallized in the normal configuration. We can conclude that the results obtained by the Raman spectroscopy confirm those found by X-ray diffraction.

3.5. UV-Vis

The diffuse reflectance spectra of all samples recorded in the range of 240–800 nm are presented in Fig. 7. For all the samples, we observe an absorption band in the UV (240–350 nm) region, which can be attributed to the band-to-band transition of the AlO_6 in the $ZnAl_2O_4$ spinel [66, 67]. Also, doped samples show stronger absorption bands in the UV and visible (450–720 nm) regions, and the absorption edge reaches 450 nm, indicating that the doped samples partially absorb in the visible region. In addition, the absorption intensity of the doped samples in the ultraviolet region increased significantly and the light-absorbing edge moved towards the longer wavelengths with the increase in the concentration of Pb^{2+}. This could be due to the interaction between La^{3+} and Pb^{2+} ions with the $ZnAl_2O_4$ matrix, which contributed to the excitation of generated carriers [68].

The bandgap energy (E_g) of the $ZnAl_2O_4$ samples can be determined from plots of $(Kh\nu)^n$ versus ($h\nu$) as shown in Fig. 8 (with $n = 2$, which is appropriate for a direct bandgap material such as $ZnAl_2O_4$) using the Tauc relation given as

$$(Kh\nu)^2 = C(h\nu - E_g), \qquad (3)$$

where K is the Kubelka–Munk function [69] given as

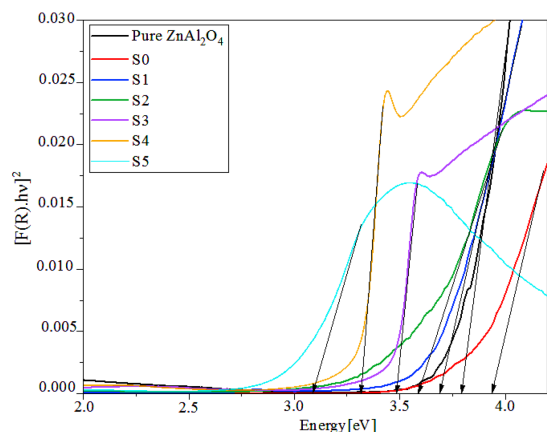$$K = \frac{(1 - R)^2}{2R} = F(R), \qquad (4)$$

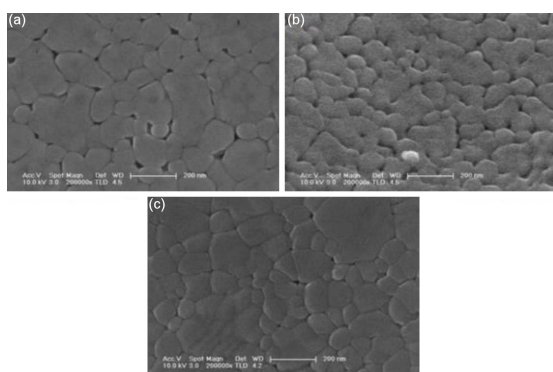Fig. 8. $(F(R)h\nu)^2$ versus $h\nu$ plots for all samples.

Fig. 9. SEM micrographs of ZnAl$_2$O$_4$ nanoparticles synthesized of the: (a) S1, (b) S2, and (c) S3 sample.

where R is reflectance (%), $h\nu$ is the photon energy, C is a proportionality constant, and E_g is the bandgap energy. The determination of the intercept on the $h\nu$ axis by extrapolating the linear part of the plot to $(Kh\nu)^2 = 0$ as shown in Fig. 8, gives the bandgap energy E_g.

It is found that the optical band gap values are: 3.95, 3.85, 3.70, 3.60, 3.48, 3.34, and 3.05 eV for pure ZnAl$_2$O$_4$, S0, S1, S2, S3, S4, and S5 samples, respectively. For pure ZnAl$_2$O$_4$, E_g is 3.95 eV which is a little higher than that previously reported where $E_g = 3.80$ eV. It is known that impurities, carrier concentration, and lattice concentration may influence the optical band gap of materials. Therefore, the observed decrease in E_g with increasing Pb^{2+} ions suggests the insertion of new energy levels between the band structures [70]. It can be concluded that these results confirm those found by X-ray diffraction.

3.6. SEM and EDX

The observation of the scanning electron micrographs (SEM) in Fig. 9 allows us to say that the morphology of the grains is irregular. It varies from a spheroid shape for small particles to an elongated
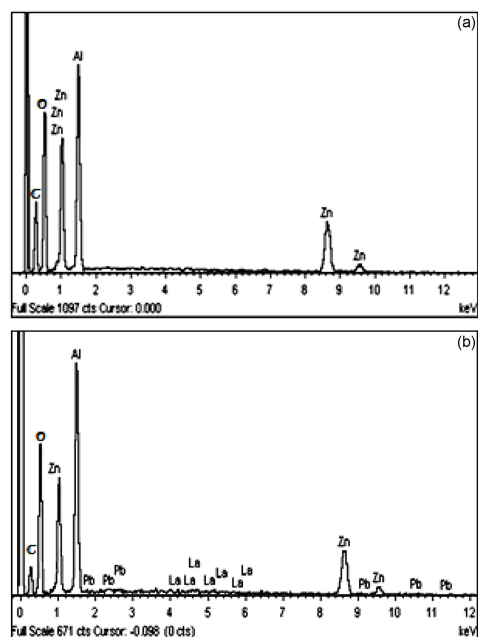

Fig. 10. EDX spectra for (a) pure ZnAl$_2$O$_4$, and (b) the S1 sample.

shape for large particles. The particle size is widely distributed with an average size of around 100 nm. This leads to conclude that the crystallites tend to agglomerate in small clusters [71], giving nanoparticles having sizes much larger than those of the crystallites [S1 (22 nm); S2 (19 nm) and S3 (24 nm)] calculated from Sherrer's formula.

Figure 10a, showing the spectrum of pure ZnAl$_2$O$_4$, clearly indicates the detection of the elements (Zn, Al, and O) present in pure zinc aluminate. Meanwhile in Fig. 10b, which represents the spectrum of the S1 sample, we note, in addition to the matrix elements, the presence of dual doping elements (La^{3+} and Pb^{2+}). Also, we observe on the other spectra which are not represented here, that the intensity of the lead peak increases with its concentration. The presence of carbon comes from the metallization of the samples.

3.7. Photocatalytic activity

As shown in Fig. 11, the degradation of HCV by direct photolysis requires what may seem in practice too long. This makes the process of little benefit for environmental applications over other methods. Our initial objective for this study was to apply the process of photocatalysis, but the results were obtained in the dark pointing that the process of adsorption is also important observations are evidenced in Fig. 12 (dye removal rate versus time). For this reason, we have examined (i) adsorption and (ii) photocatalysis. Experimentally, the only difference between the two processes is the absence and presence of ultraviolet radiation in the adsorption and photocatalysis, respectively.
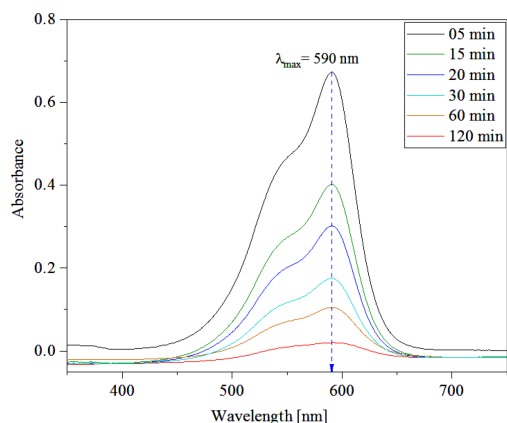
Fig. 11. The absorbance of HCV in the presence of ZnAl$_2$O$_4$.

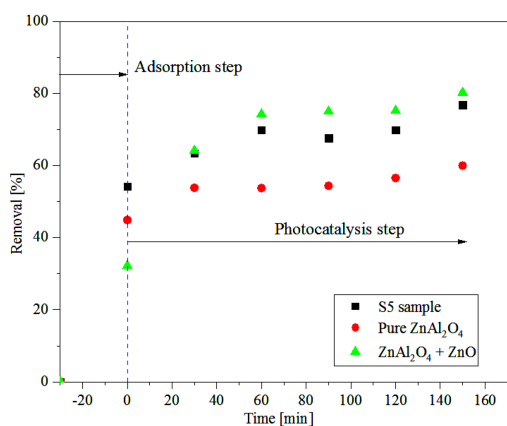Fig. 12. Dye removal rate versus time.

Figure 13a–c represents the photocatalytic activity of pure ZnAl$_2$O$_4$, S5 sample, and ZnAl$_2$O$_4$/ZnO respectively. By comparing the results obtained with those of direct photolysis, it is clear that the addition of ZnAl$_2$O$_4$ powder of different types in the reaction medium considerably accelerates the degradation of the dye.

After 120 min of irradiation, 75%, 70%, and 57% of the dye are degraded by (ZnAl$_2$O$_4$/ ZnO), S5, and pure ZnAl$_2$O$_4$, respectively. The difference in dye removal rate depends on the used powder. Pure ZnAl$_2$O$_4$ is the least efficient catalyst. However, the presence of Pb^{2+} and ZnO, respectively, in the other two samples S5 and (ZnAl$_2$O$_4$/ZnO), makes them more potent.

This is since the atoms of lead replace the atoms of Zn, which creates surface exchanges and an increase in the lattice parameter as well as a decrease in gap energy (3 eV), making the S5 sample more powerful and efficient than pure ZnAl$_2$O$_4$ (E_g = 3.8 eV). Indeed, Tangcharoen et al. [72] showed that the energy of the bandgap significantly influences the photocatalytic activity of aluminate spinels; the lower the energy of the bandgap, the better the photocatalytic activity.
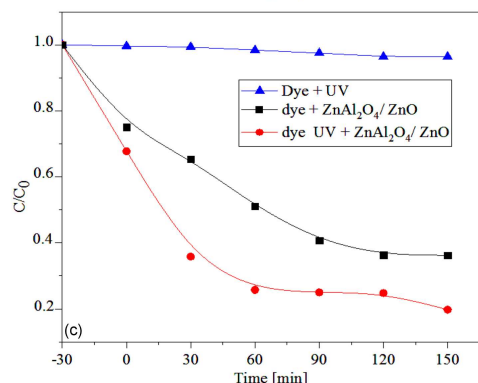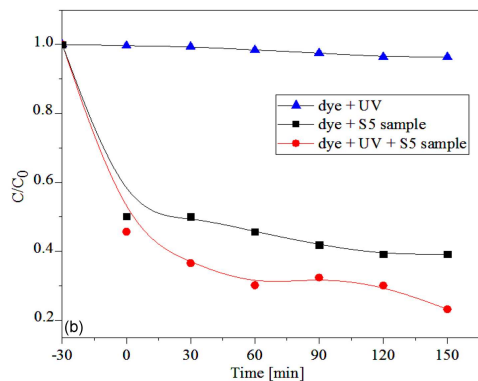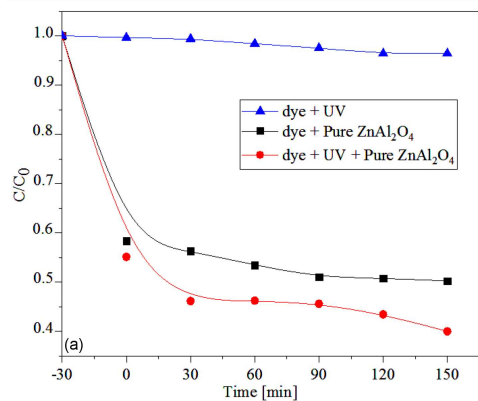

Fig. 13. Photocatalytic activity of: (a) pure ZnAl$_2$O$_4$, (b) S5 sample, (c) ZnAl$_2$O$_4$/ZnO.

As for ZnAl$_2$O$_4$/ZnO, it is the most efficient thanks to its bandgap energy (3 eV), and its excitonic energy of 60 meV [73]. The highest value of all semiconductors, and may also be due to the intervention of other factors such as particle size, specific surface area and particle morphology, which could be introduced by the addition of ZnO to the spinel ZnAl$_2$O$_4$, and whose photocatalytic behavior depends considerably on it.

3.8. Discussion on the photocatalytic activity

The photon excitation of ZnAl$_2$O$_4$ amounts to creating electron–hole pairs, that is, a redox system, bypassing the electrons (e$^-$) from the valence band (VB) to the conduction band (CB) creating a hole (h$^+$) in the VB.

The created holes move to the surface of the material where their high oxidizing power manifests itself towards the adsorbed oxidizable species, while the produced electrons act on the reducible adsorbed species. It is accepted that in an aerated environment, the electrons, which have acquired the energy of the conduction band, are captured by the adsorbed oxygen to give superoxide radical ions and a new equilibrium state is established on the spinel surface [74, 75]. This prevents electron–hole recombination, and thus allows hydroxyl and superoxide radicals to react with HCV.

The mechanism of photocatalysis includes the following reactions

$$\text{used powder} + h\nu \rightarrow \text{used powder} + \text{h}^+ + \text{e}^-,$$

$$H_2O + \text{h}^+ \rightarrow^\bullet OH + H^+,$$

$$OH^- + \text{h}^+ \rightarrow^\bullet OH,$$

$$O_2 + \text{e}^- \rightarrow O_2^{\bullet-},$$

$$HCV(P) +^\bullet OH(O_2^{\bullet-}) \rightarrow H_2O + CO_2$$

$$+\text{degradation products.} \quad (5)$$
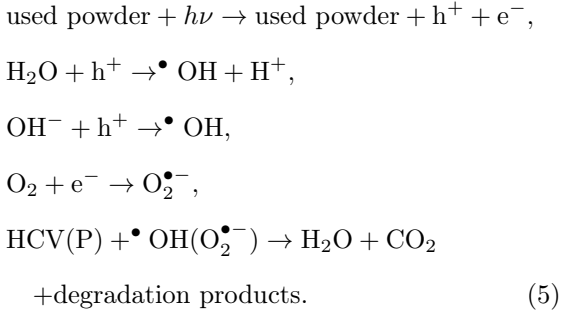
3.9. Adsorption activity

Figure 14 indicates the monitoring of the adsorbed quantity as a function of the contact time (under the same conditions as for photocatalysis). The adsorption quantity was calculated according to

$$Q_{\text{ads}} = \frac{V(C_0 - C_e)}{m_{\text{adsorbent}}}, \quad (6)$$

where C_0 is the initial concentration of HCV, C_e is the equilibrium concentration of the solution, V is the volume of solution, and $m_{\text{adsorbent}}$ is the mass of adsorbent (pure $ZnAl_2O_4$, S5, and $ZnAl_2O_4/ZnO$).

Its examination makes it possible to conclude that the adsorption is remarkable for the three samples, and the adsorption amount after 30 min is 1.63, 1.35, and 0.96 mg/g for sample S5, pure $ZnAl_2O_4$, and $ZnAl_2O_4/ZnO$, respectively. At 150 min of contact, the remaining quantity of HCV decreases, and the amount adsorbed was found to be 2.25, 2.09, and 1.69 mg/g in the presence of $ZnAl_2O_4/ZnO$, S5, and pure $ZnAl_2O_4$, respectively.

In the case of pure and doped $ZnAl_2O_4$, the curves have two important parts: between 0 and 30 min, the curve is linear, there is rapid adsorption with a high speed, and is more important for S5. After 30 min of contact, the adsorption decreases with a lower speed.

This is explained by the rapid fixation of the molecules in the first moments because, in addition to the presence of surface pores, there is a great affinity between the molecules of the dye and the adsorbent. The formation of the kinetic plateau ($m_{\text{HCV}}/m_{\text{adsorbent}}$) informs us that all the pores are occupied by molecules of HCV.
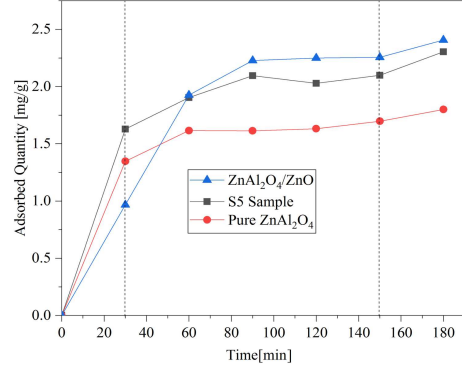

Fig. 14. Adsorption activity of the pure $ZnAl_2O_4$, S5 sample and $ZnAlO_4/ZnO$.

Concerning the $ZnAl_2O_4/ZnO$ sample, the adsorption is slow because, from the first moments of contact up to 150 min, the HCV molecules slowly bind to the surface because there is a lack of affinity between ZnO and HCV molecules.

We found that the adsorption quantity of HCV molecules is higher for the samples of S5 and pure $ZnAl_2O_4$ than for the sample $ZnAl_2O_4/ZnO$. The affinity between the adsorbate and the adsorbent and the adsorbents surfaces strongly influence the binding performance, i.e., the fixation speed of the HCV molecules. We observe that after 150 min the curves of the three samples have a flat level. Therefore, we can conclude the adsorption of the three samples follows the Langmuir isotherm model.

4. Conclusion

$ZnAl_2O_4$: (1% La^{3+}, x% Pb^{2+} $x = 0 - 2.5$) powders were successfully prepared by the citrate sol–gel technique. The X-ray diffraction, Raman spectroscopy, and FTIR results confirmed that all the samples prepared to consist of a single-phase cubic spinel structure with no other impurity phases. In addition, TG/DSC combined analysis shows that the complete crystallization of the spinel takes place around 820°C, which validates our choice of the calcination temperature (900°C). The average crystallite size and lattice parameter decrease with increasing Pb^{2+} doping concentration up to 1.5 mol%. Beyond this value considered as optimal, Vegard's law is verified, i.e., the lattice parameter of samples increases with increasing doping concentration. The morphology of the grains is irregular. It varies from a spheroid shape for small particles to an elongated shape for large particles, with an average size of around 100 nm. This leads to conclude that the crystallites tend to agglomerate in small clusters, giving nanoparticles having sizes much larger than those of the crystallites (19–25 nm) calculated from Scherrer's formula. Furthermore, UV–Vis spectra analysis indicates that with the increase in the concentration of Pb^{2+} ions, the bandgap of the doped sample decreases and exhibits a redshift. This clearly shows that the doping ions Pb^{2+} are

incorporated into the ZnAl$_2$O$_4$ matrix, introducing new energy levels into the forbidden band. Finally, the photocatalytic study of different samples of ZnAl$_2$O$_4$ shows that they can be used as good adsorbents for the degradation of the hexamethyl violet dye crystallized in an aqueous solution.

Acknowledgments

References

[1] S. Battiston, C. Rigo, E. da C. Severo, M.A. Mazutti, R.C. Kuhn, A. Gündel, E.L. Foletto, *Mater. Res.* **17**, 734 (2014).

[2] S.F. Wang, G.Z. Sun, L.M. Fang, L. Lei, X. Xiang, X.T. Zu, *Sci. Rep.* **5**, 12849 (2015).

[3] M. Shahmirzaee, M. Shafiee Afarani, A.M. Arabi, A. Iran Nejhad, *Res. Chem. Intermed.* **43**, 321 (2016).

[4] X. Li, Z. Zhu, Q. Zhao, L. Wang, *J. Hazard. Mater.* **186**, 2089 (2011).

[5] L. Zhang, J. Yan, M. Zhou, Y. Yang, Y.-N. Liu, *Appl. Surf. Sci.* **268**, 237 (2013).

[6] M. Dhinagaran, V. Elakkiya, S. Sumathi, *Opt. Mater.* **111**, 110546 (2021).

[7] R. Ianoş, S. Borcănescu, R. Lazău, *Chem. Eng. J.* **240**, 260 (2014).

[8] E. Huízar-Padilla, H. Guillén-Bonilla, A. Guillén-Bonilla, V.M. Rodríguez-Betancourtt, A. Sánchez-Martínez, J.T. Guillen-Bonilla, L. Gildo-Ortiz, J. Reyes-Gómez, *Sensors* **21**, 2362 (2021).

[9] X. Huang, X. Wei, Y. Zeng, et al., *Nanoscale* **13**, 8514 (2021).

[10] M.-T. Tsai, Y.-S. Chang, I.-B. Huang, B.-Y. Pan, *Ceram. Int.* **39**, 3691 (2013).

[11] W. Mekprasarta, K. Boonyarattanakalina, W. Pecharapaa, K.N. Ishiharab, *Mater. Today Proc.* **5**, 14126 (2018).

[12] D.P. Dutta, R. Ghildiyal, A.K. Tyagi, *J. Phys. Chem. C* **113**, 16954 (2009).

[13] E.L. Foletto, S. Battiston, J.M. Simões, M.M. Bassaco, L.S.F. Pereira, E.M. de Moraes Flores, E.Ir. Müller, *Micropor. Mesopor. Mater.* **163**, 29 (2012).

[14] L. Zhao, X.Y. Li, J. Zhao, *Fabricat. Adv. Mater. Res.* **518-523**, 736 (2012).

[15] X. Zhao, L. Wang, X. Xu, X. Lei, S. Xu, F. Zhang, *AIChE J.* **58**, 573 (2012).

[16] R. Huo, Y. Kuang, Z. Zhao, F. Zhang, S. Xu, *J. Coll. Interface Sci.* **407**, 17 (2013).

[17] T.R. Gurugubelli, B. Babu, J. Kim, K. Yoo, *Chem. Papers* **75**, 6407 (2021) (2021).

[18] C. Lu, Z. Wei, H. Qiao, X. Wu, H. Zhang, J. Shi, S. Huang, *J. Electron. Mater.* **49**, 6536 (2020).

[19] R. Mahajan, S. Kumar, R. Prakash, V. Kumar, *AIP Conf. Proc.* **1953**, 030209 (2018).

[20] R. Prakash, S. Kumar, R. Mahajan, P. Khajuria, V. Kumar, R.J. Choudhary, D.M. Phase, *AIP Conf. Proc.* **1953**, 030040 (2018).

[21] M.K. Hussen, F. B. Dejene, M. Tsega, *J. Mater. Sci. Mater. Electron.* **30**, 10191 (2019).

[22] A.V. Belyaev, M.I. Lelet, N.I. Kirillova, N.M. Khamaletdinova, M.S. Boldin, A.A. Murashov, S.S. Balabanov, *Ceram. Int.* **45**, 4835 (2019).

[23] D. Zhang, B. Zhu, S. Ren, Q. Wang, Q. Wang, S. Li, B. Zhang, W. Wang, *Mater. Res. Express* **8**, 025902 (2021).

[24] S. Siragam, R.S. Dubey, L. Pappula, *Mater. Today Proc.* **45**, 2091 (2021).

[25] B. Zhu, S. Ren, D. Zhang et al., *J. Lumin.* **239**, 118362 (2021).

[26] V. Singh, N. Singh, M.S. Pathak, V. Dubey, P.K. Singh, *Optik* **155**, 285 (2018).

[27] S.A. Mirbagheri, S.M. Masoudpanah, S. Alamolhoda, *Optik* **204**, 164170 (2020).

[28] R. Priya, A. Negi, S. Singla, O.P. Pandey, *Optik* **204**, 164173 (2020).

[29] P. Mohanty, S. Mohapatro, R. Mahapatra, D.K. Mishra, *Mater. Today Proc.* **35**, 130 (2021).

[30] N. Vinitha, J. Baby, K.M. Krishna, *AIP Conf. Proc.* **2082**, 030034 (2019).

[31] S. Siara, C. Elvis, R. Harishkumar, P.V. Chellam, *Mater. Res. Bull.* **145**, 111530 (2022).

[32] P.K. Haldar, T.K. Parya, S. Mukhopadhyay, *Int. Ceram. Rev.* **69**, 44 (2020).

[33] D. Zhang, Y.H. Qiu, Y.R. Xie, X.C. Zhou, Q.R. Wang, Q. Shi, S.H. Li, W.J. Wang, *Mater. Des.* **115**, 37 (2017).

[34] F. Femila Komahal, H. Nagabhushana, R.B. Basavaraj, G.P. Darshan, B. Daruka Prasad, *Opt. Mater.* **84**, 536 (2018).

[35] D. Zhang, X. Ma, Q. Zhang, Y. Xie, Q. Shi, Q. Wang, W. Wang, *J. Alloys Compd.* **688**, 581 (2016).

[36] Y. Chenga, K. Suna, P. Ge, *Optik* **170**, 1 (2018).

[37] Q. Lu, Z. Wei, X. Wu, S. Huang, M. Ding, J. Ma, *Chem. Phys. Lett.* **772**, 138582 (2021).

[38] W. Somraksa, S. Suwanboon, P. Amorn-pitoksuk, C. Randorn, *Mater. Res.* **23**, 0627 (2020).

[39] S. Huang, Z. Wei, X. Wu, J. Shi, *J. Alloys Compd.* **825**, 154004 (2020).

[40] M.T. Tran, D.Q. Trung, Nguyen Tu, *J. Alloys Compd.* **884**, 161077 (2021).

[41] S. Siragam, R.S. Dubey, L. Pappula, *Mater. Today Proc.* **45**, 2091 (2021).

[42] J. Liu, W. Zhou, D. Jiang, D. Wang, W. Wu, Y. Wang, X. Ma, *Catal. Today* **368**, 58 (2020).

[43] V. Elakkiya, S. Sumathi, *J. Alloys Compd.* **820**, 153174 (2020).

[44] V. Singh, M.K. Tiwari, *Optik* **206**, 163600 (2020).

[45] G. Fournet, *J. Phys. Radium* **14**, 374 (1953).

[46] V.A. Lubarda, *Mech. Mater.* **35**, 53 (2003).

[47] S.V. Motloung, F.B. Dejene, H.C. Swart, O.M. Ntwaeaborwa, *J. Sol-Gel Sci. Technol.* **70**, 422 (2014).

[48] M. Ding, Z. Wei, K. Li, X. Wu, J. Shi, S. Huang, *J. Ceram. Soc. Jpn.* **128**, 927 (2020).

[49] M. Jain, Manju, A. Gundimeda, et al., *J. Alloys Compd.* **797**, 148 (2019).

[50] R. Yuvasravana, P.P. George, N. Devanna, *Mater. Today Proc.* **4**, 10664 (2017).

[51] W. Staszak, M. Zawadzki, J. Okal, *J. Alloys Compd.* **492**, 500 (2010).

[52] X. Wu, Z. Wei, X. Chen, X. Wang, H. Yang, J. Jiang, L. Yuan, *Russ. J. Phys. Chem. A* **91**, 2651 (2017).

[53] A. Saffar, H.A. Ahangar, S. Salehi, M.H. Fekri, A. Rabbani, *J. Sol-Gel Sci. Technol.* **99**, 158 (2021).

[54] S.G. Menon, K.S. Choudhari, S.A. Shivashankar, C. Santhosh, S.D. Kulkarni, *J. Alloys Compd.* **728**, 484 (2017).

[55] Z. Chen, X. Zhao, S. Wei, *Optik Int. J. Light Electron. Opt.* **242**, 167151 (2021).

[56] R. Ianos, R. Lazau, I. Lazau, C. Pacurariu, *J. Europ. Ceram. Soc.* **32**, 1605 (2012).

[57] F. Ercan, T. Ates, O. Kaygili, N. Bulut, S. Koytepe, F. Alahmari, I. Ercan, A.H. Hssain, *J. Austral. Ceram. Soc.* **57**, 1155 (2021).

[58] V. D'Ippolito, G.B. Andreozzi, F. Bosi, U. Halenius, L. Mantovani, D. Bersani, R.A. Fregola, *Mineralog. Mag.* **77**, 2941 (2013).

[59] R.E. Rojas-Hernandez, F. Rubio-Marcos, G. Gorni, C. Marini, M. Danilson, L. Pascual, R.U. Ichikawa, I. Hussainova, J.F. Fernandez, *Mater. Chem. C* **9**, 657 (2021).

[60] A. Chopelas, A.M. Hofrmeister, *Phys. Chem. Miner.* **18**, 279 (1991).

[61] C.M. Fang, C.K. Loong, G.A. de Wijs, G. de With, *Phys. Rev. B* **66**, 144301 (2002).

[62] V. D'Ippolito, G.B. Andreozzi, D. Bersani, P.P. Lotti, *J. Raman Spectrosc.* **46**, 1255 (2015).

[63] S. Suwanboon, P. Amornpitoksuk, T. Rattana, C. Randorn, *Ceram. Int.* **46**, 21958 (2020).

[64] J. Wang, A. Wang, D. Hu, X. Wu, Y. Liu, T. Chen, *Mater. Chem. Phys.* **239**, 122319 (2020).

[65] D. Dwibedi, C. Murugesan, M. Leskes, P. Barpanda, *Mater. Res. Bull.* **98**, 219 (2018).

[66] S.V. Motloung, F.B. Dejene, H.C. Swart, O.M. Ntwaeaborwa, *Ceram. Int.* **41**, 6776 (2015).

[67] S.V. Motloung, F.B. Dejene, L.F. Koao, O.M. Ntwaeaborwa, *Opt. Mater.* **64**, 26 (2017).

[68] S. Yuvaraj, N. Manikandan, G. Vinitha, *Mater. Res. Express* **4**, 115027 (2017).

[69] Q. Tian, M. Ran, G. Fang, L. Ding, A. Pan, K. Shen, Y. Deng, *Separat. Purificat. Technol.* **239**, 116574 (2020.

[70] S.V. Motloung, M. Tsega, F.B. Dejene, H.C. Swart, O.M. Ntwaeaborwa, L.F. Koao, T.E. Motaung, M.J. Hato, *J. Alloys Compd.* **677**, 72 (2016).

[71] S.V. Motloung, F.B. Dejene, H.C. Swart, O.M. Ntwaeaborwa, *J. Lumin.* **163**, 8 (2015).

[72] T. Tangcharoen, J. T-Thienprasert, C. Kongmark, *J. Mater. Sci. Mater. Electron.* **29**, 8995 (2018).

[73] N. Kamarulzaman, M.F. Kasim, R. Rusdi, *Nanoscale Res. Lett.* **10**, 346 (2015).

[74] A. Chaudhary, A. Mohammad, S.M. Mobin, *Mater. Sci. Eng. B* **227**, 136 (2018).

[75] T. Tangcharoen, J. T-Thienprasert, C. Kongmark, *Int. J. Appl. Ceram. Technol.* **18**, 1125 (2021).